Soft Matter

PAPER

Shear-induced macroscopic "Siamese" twins in soft colloidal crystals†

Sara Mehdizadeh Taheri,[a] Sabine Rosenfeldt,[a] Steffen Fischer,[a] Peter Bösecke,[b] Theyencheri Narayanan,[b] Peter Lindner[c] and Stephan Förster*[a]

Soft colloidal crystals are inherently highly susceptible to shear. We find by using scanning rheo-SANS and scanning synchrotron-rheo-SAXS experiments that high shear strains cause macroscopic "Siamese" twinning in lyotropic FCC-crystals formed by block copolymer micelles or polymer-coated nanoparticles. The twins extend over the whole gap of the shear cell with one twin always located in the outer region of the gap, and the other twin always located in the inner region of the gap. We could visualize twin boundary surfaces by using transmission electron microscopy. In analogy to the plastic deformation of nanocrystalline metals under high shear stress and high deformation rates we propose a deformation twining mechanism for the formation of such macroscopic twins.

Introduction

Soft materials like polymers and gels can form highly ordered soft crystals such as for lyotropic and thermotropic liquid crystalline phases.[1,2] These crystals consist of building blocks such as micelles or mesogens that interact *via* soft interaction potentials. These are characterized by a potential energy comparable to the thermal energy, and a weak spatial dependence of the potential which for very soft systems only logarithmically depends on distance.[3,4] This enables soft building blocks to easily order, thereby tolerating imperfections in size and shape, as well as lattice imperfections such as defects and distortions because the related increase in potential energy is very small. Imperfections limit the spatial coherence of the crystalline lattice. Soft crystals typically consist of relatively small, well-ordered domains of typically 10–20 lattice periods dimension, which corresponds to typical domain sizes in the range of 50–500 nm.

The mechanical properties of soft crystals are largely determined by the number and mobility of the defects. A special defect is the occurrence of twins, where two adjacent crystals share common lattice points in a symmetrical manner such that a twin boundary surface exists between the two crystals. FCC-crystals, which are often found in lyotropic systems, can exist in two different stacking orders of the (111)-planes corresponding to ABCAB… or ACBACB… stacking, which are the respective twins. Usually, twins or twinned domains occur as small adjacent grains within large multidomain crystals.

Shear-experiments on ordered colloidal solutions and lyotropic phases were pioneered by Ackerson and Loose who first reported shear-orientation of colloidal FCC-crystals and thereby identified the layer sliding mechanism.[4–6] The generation of FCC long-range order by shear for block copolymer micelles was first demonstrated by McConnell and Gast[7] using rheo-SANS experiments under steady shear. The work on the structure and flow behaviour of colloidal crystals and block copolymer micelles has been reviewed by Hamley.[8]

Most relevant for the present studies is a series of papers from Diat *et al.* who investigated the shear-alignment of FCC block copolymer micelles by synchrotron rheo-SAXS which for the first time allowed investigation of the structure formed in the shear cell not only in the "radial" beam position, probing the [111]-direction of the FCC-lattice as in previous experiments, but also in the "tangential" position, which probes the [110]-direction that is relevant for the identification of twins.[9,10] After continuous shear the samples were annealed by oscillatory shear. The authors reported for the first time the existence of fully separated twin single crystals, each coherent on the millimetre scale. This was possible by using a small 0.2 mm diameter X-ray beam that allowed probing in the "tangential" position the centre of the gap as well as the outer region of the gap of the Searle cell. In the centre of the gap the experiment showed both twins, whereas close to the outer region of the gap, just one of the two twins was observed. They estimated that about half of the gap (in thickness) was occupied by one twin and the other half by the second twin. Recently the tangential direction could also be probed by rheo-SANS, similarly by observing a pure macroscopic twin after cessation of shear.[11]

[a]Physical Chemistry I, University of Bayreuth, 95440 Bayreuth, Germany. E-mail: stephan.foerster@uni-bayreuth.de; Fax: +49 921 552760; Tel: +49 921 552760

[b]European Synchrotron Research Facility (ESRF), 38000 Grenoble, France. E-mail: narayan@esrf.fr; Fax: +33 (0) 47688 2325; Tel: +33 (0) 47688 2121

[c]Institut-Laue-Langevin (ILL), 38000 Grenoble, France. E-mail: lindner@ill.eu; Fax: +33 (0) 47620 7120; Tel: +33 (0) 47620 7180

† Electronic supplementary information (ESI) available. See DOI: 10.1039/c3sm51075a

With recent progress in SANS and synchrotron SAXS instrumentation it has become possible to probe samples with smaller neutron and X-ray beams, allowing scanning through the gap of shear cells with higher resolution. Here we report such rheo-SANS and synchrotron rheo-SAXS studies on highly ordered lyotropic FCC-crystals formed by block copolymer micelles and by polymer-coated nanoparticles. We used small, *i.e.* 300 μm diameter neutron and 200 μm diameter X-ray beams to scan across the gap of the shear cell to probe the twin structure and possibly locate twin boundary surfaces. As the shear history of such non-linear viscoelastic samples is of importance, we employ a well-defined shear protocol where the samples are first sheared with a constant shear-rate between 200 and 1000 s^{-1} until the measured scattering patterns were stationary and constant with time. Then shearing was abruptly stopped to induce twin-formation. This sequence leads to well reproducible results. We observe that macroscopic "Siamese" twins are formed in the gap of the shear cell with the twin boundary surface located between the centre and the inner wall of the gap. Twin boundary surfaces can be directly imaged by transmission electron microscopy of chemically vitrified samples. We propose a possible twinning mechanism that is motivated by recent investigations of mechanical twin formation during plastic deformation of nanocrystalline metals under high stress and deformation rates.

Experimental part

PI-PEO synthesis

Poly(isoprene-*b*-ethylene-oxides) (PI-PEO) were synthesized by sequential living anionic polymerization of isoprene and ethylene oxide initiated by *sec*-butyl lithium in THF at −70 °C. After completion of the PI-polymerization the living end groups were reacted with ethylene oxide to obtain terminal –OH-end groups. The OH-groups were deprotonated with diphenylmethyl-potassium (DPMK) to initiate the polymerization of ethylene oxide to obtain PI-PEO. The degrees of polymerisation of the PI-PEOs used for the experiments are $N_{PI} = 62$ and $N_{PEO} = 193$ and with a polydispersity of $M_w/M_n = 1.03$ (sample ID PI-PEO-1) and $N_{PI} = 55$ and $N_{PEO} = 170$ and with a polydispersity of $M_w/M_n = 1.01$ (sample ID PI-PEO-14). The polymers were characterized by GPC and ^{1}H-NMR. In the following, the numbers in brackets indicate the degree of polymerization.

Sample preparation

For the experiments we used 13–16 wt% solutions of PI-PEO in D_2O (SANS) or H_2O (SAXS). In water PI-PEO forms spherical micelles with a micellar core consisting of PI-blocks and a micellar shell consisting of water-soluble PEO-blocks. At concentrations between 10 and 25% the micelles form highly ordered lyotropic liquid crystalline FCC-phases. For the experiments the block copolymers were directly dissolved in D_2O or H_2O and equilibrated for 2 days to obtain clear homogeneous gels.

Lyotropic nanoparticle phase

The synthesis of the polystyrene-coated Fe_2O_3-nanoparticles has been described elsewhere.[12] For the experiments we used nanoparticles with a diameter of 16.6 nm coated with a spherical brush-like polystyrene layer of molecular weight 28 000 g mol^{-1} at 50 wt% in toluene where the nanoparticles form a highly ordered FCC-phase.

Transmission electron microscopy

To image the PI-PEO lyotropic crystal structure by transmission electron microscopy, we chemically templated the sample structure by hydrolyzing tetramethoxysilane (TMOS) under acidic conditions in the aqueous phase of the sample, followed by calcination to remove the organic components. Details of this preparation are outlined in ref. 13. The procedure yields a mesoporous silica sample that is a replica of the lyotropic phase. The silica was then imaged using a Phillips CM 300 electron microscope.

Rheo-SANS and synchrotron rheo-SAXS experiments

The synchrotron rheo-SAXS experiments were performed at the beamline ID02 at the European Synchrotron Radiation Facility (ESRF, Grenoble, France). Rheo-SANS experiments were performed at the instrument D11 at the Institut Laue-Langevin (ILL, Grenoble, France). For the shear-experiments at ILL we used a Bohlin CVO 120 HR stress-controlled rheometer with a Searle-type quartz shear cell having a 1 mm gap between the inner rotor (radius: 23 mm, height: 60 mm) and the outer stator (radius 24 mm). For the shear-experiments at ESFR we used an RS300 stress-controlled rheometer with a Searle-type polycarbonate shear cell having a 1 mm gap between the inner rotor (radius: 10 mm, height: 40 mm) and the outer stator (radius: 11 mm). The wall thickness around the beam position is 100 μm. The viscous gel-like samples were filled into the gap and shear-aligned at shear rates of 200–1000 s^{-1} for 5–30 seconds. Abrupt cessation of shear enables trapping the structure that has been formed in the shear cell. The structure of the sample in the shear cell was then scanned with a neutron beam of 10 mm vertical and 0.3 mm horizontal diameter defined by a vertical slit aperture. The wavelength was $\lambda = 0.6$ nm with a wavelength distribution (FWHM) of 9%. Details of the instrument and the data reduction using the standard software of the instrument can be found in ref. 14. At ID02 a FreLoN CCD detector was used.[15] The X-ray wavelength was $\lambda = 0.1$ nm. The sample was scanned with an X-ray beam of 0.2 mm horizontal and 0.4 mm vertical diameter.

SANS-scattering patterns show considerably larger smearing compared to SAXS-scattering patterns due to the wavelength distribution of the neutron beam, the limited primary beam collimation, and the finite diameter of the neutron beam. For the present experiments we have made considerable efforts to minimize these contributions by choosing a wavelength selector setting leading to only 9% wavelength spread (FWHM), 20.5 m collimation length, and a horizontal beam diameter of 300 μm by using a slit aperture. Since these settings considerably decrease the neutron beam intensity, they were a compromise between having a sufficient signal-to-noise ratio and minimum instrumental smearing. The remaining instrumental smearing was not taken into account in the model calculations.

To fill the gap of the rheometers requires between 2 and 10 ml of sample. Since the nanoparticle samples were not available in such quantities we shear-oriented the sample in the gap between two co-axially aligned capillaries (Hilgenberg, Germany). The inner capillary had a diameter of 1 mm, and the outer capillary of 2 mm, both with a wall thickness of 0.1 mm.

Scattering curves of ordered particle systems

In the following we outline the calculation of scattering patterns of oriented crystalline arrays of spherical colloids dispersed in a solvent. For two-phase systems consisting of particles (phase "1") with scattering length b_1 and volume fraction ϕ_1 in a solvent (phase "2") of scattering length b_2 and a volume fraction $\phi_2 = 1 - \phi_1$, separated by sharp interfaces, the scattered intensity per unit volume is given by[16,17]

$$I(q) = (b_1 - b_2)^2 \rho_N P(q,R)[1 + \beta(q,R)(Z(q,g) - 1)G(q,g)] \quad (1)$$

where

$$P(q,R) = \langle F^2(q,R) \rangle_R \quad (2)$$

is the particle form factor, $F(q)$ is the scattering amplitude or Fourier transform of the particle form, $\rho_N = N/V$ is the number density of the particles, $Z(q)$ is the lattice factor describing the spatial distribution of the particles, q is the scattering vector, $q = |q|$ is the modulus of the scattering vector, and $G(q)$ is the Debye–Waller factor. $\langle \ldots \rangle_R$ denotes the average over the distributions of radii R. The ratio $\beta(q)$ is given by

$$\beta(q,R) = \frac{\langle F(q,R) \rangle_R^2}{\langle F^2(q,R) \rangle_R} \quad (3)$$

The effect of the ratio $\beta(q,R)$ on the scattered intensity is similar to the Debye–Waller factor, resulting in a decay of the Bragg-intensities with increasing scattering vector q. Eqn (1) considers the effect of the particles – via their first and second moments of the particle size distribution – and of the lattice – via the first and second moments of the distribution of lattice points – on the scattered intensity $I(q)$.

The scattering amplitude for spheres of radius R is given by

$$F(q,R) = \frac{3}{(qR)^3}(\sin(qR) - qR\cos(qR)) \quad (4)$$

For the calculation of the average over the size distribution the Schulz-Zimm distribution is used, which yields for the z-average of a function $f(q,R)$

$$\langle f(q,R) \rangle_R = \int_0^\infty f(q,R) R^m h(R) \, dR \quad (5)$$

with

$$h(R) = \frac{(z+1)^{z+m+1} R^z}{\bar{R}^{z+m+1} \Gamma(z+m+1)} \exp\left[-(z+1)\frac{R}{\bar{R}}\right] \quad (6)$$

and $m = 6$ is the weighting factor for the radius R, the average radius $\bar{R}$, and the relative standard deviation $\sigma_R = (z+1)^{-1/2}$.

Table 1 Reciprocal space base vectors for the two twins of an FCC-lattice. e_x, e_y, and e_z are the unit vectors in the lab-based Cartesian coordinate system

Twin	a^*	b^*	c^*
ABCA…	$\dfrac{2\pi}{a}e_x$	$\dfrac{2\pi}{a}e_y$	$\dfrac{2\pi}{a}e_z$
ACBA…	$\dfrac{2\pi}{3a}(2e_x - e_y + 2e_z)$	$\dfrac{2\pi}{3a}(2e_x + 2e_y - e_z)$	$\dfrac{2\pi}{3a}(-e_x + 2e_y + 2e_z)$

The distribution is normalized such that $\int_0^\infty R^m h(R) \, dR = 1$. The use of a Schulz-Zimm distribution has the advantage to yield analytical expressions for $\langle P(q) \rangle$, $\langle F(q) \rangle$, and $\beta(q)$.[16]

Using the Miller indices (hkl) for a given crystal lattice plane, the lattice factor for an ideal undistorted lattice can be written as

$$Z(q,g) = \frac{(2\pi)^3}{nv} \sum_{\substack{h,k,l=-\infty \\ (hkl) \neq (000)}}^{\infty} f_{hkl}^2 L_{hkl}(q, g_{hkl}) \quad (7)$$

where n is the number of particles per unit cell, f_{hkl} is the structure factor of the unit cell, v is the volume of the unit cell, and $L_{hkl}(q,g_{hkl})$ is a normalized peak shape function that depends on the reciprocal lattice vectors g_{hkl}. The summation is over all values of the Miller indices (hkl) except for $(hkl) = (000)$ to ensure that the calculated Porod invariant is given by $(2\pi)^{-3}V \int I(q) \, dq = Q = \phi_1(1 - \phi_1)$.

The structure factor for an FCC-lattice is given by

$$f_{hkl} = 1 + \cos[\pi(h+k)] + \cos[\pi(h+l)] + \cos[\pi(k+l)] \quad (8)$$

which reduces to

$$f_{hkl} = \begin{cases} 4 & \text{for} \quad h,k,l \text{ all even } \vee h,k,l \text{ all odd} \\ 0 & \text{else} \end{cases}$$

The reciprocal lattice vector g_{hkl} is given by

$$g_{hkl} = ha^* + kb^* + lc^* \quad (9)$$

where a^*, b^*, c^* are the base vectors of the reciprocal lattice. For the two possible twins of an FCC-lattice, the unit cells are oriented differently in space. The corresponding base vectors are given in Table 1. In Fig. 1 the spatial orientation of the unit cells corresponding to both twins is defined, which is needed for the calculation of the scattering patterns. The location and orientation of the twinned unit cell (twin "B") can be obtained from the original unit cell (twin "A") via a rotation around its [111]-axis by an angle of 60°.

The Debye–Waller factor $G(q)$ is given by

$$G(q) = \exp[-\sigma_a^2 \bar{a}^2 q^2] \quad (10)$$

where $\bar{a} = \dfrac{1}{\sqrt{2}}a$ is the next nearest neighbour distance between adjacent particles for a FCC-lattice. For the peak shape function we consider a normalized Gaussian
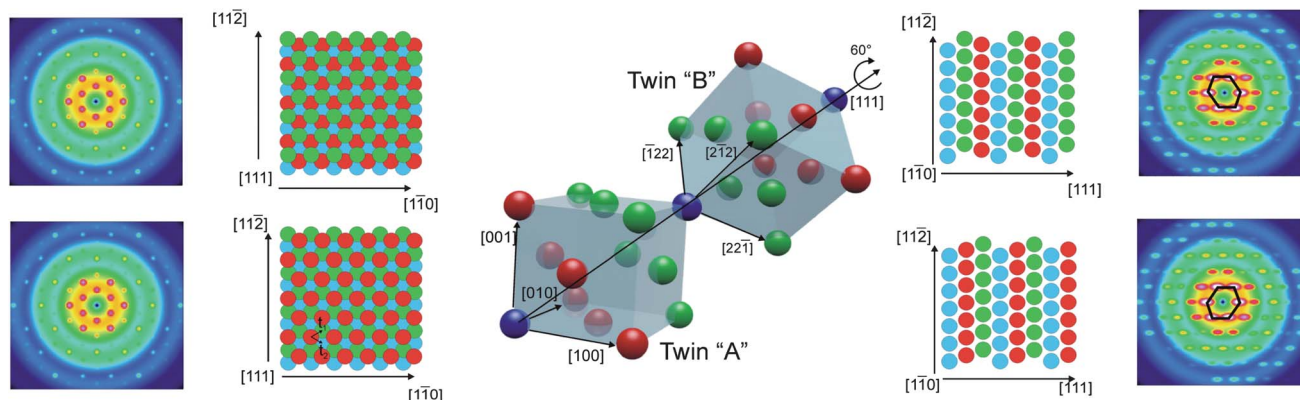
Fig. 1 FCC-unit cells for twin "A" and twin "B". The unit cell of twin "B" is obtained from twin "A" by a 60° rotation around the [111]-axis. Also shown are the stacking orders for the "radial" beam position (left) and the "tangential" beam position (right) for twin "A" (lower panel) and for twin "B" (upper panel). For the respective stacking orders the corresponding scattering patterns are calculated. The two different distorted hexagonal arrays of the first-order reflections in the "tangential" beam position are highlighted on the right. They serve to distinguish both twins in the scattering experiments.

$$L(q, g_{hkl}) = \frac{8}{\pi^3 \sigma_x \sigma_y \sigma_z} \exp\left[-\frac{4}{\pi} \left(\frac{(q_x - g_{x,hkl})^2}{\sigma_x^2} + \frac{(q_y - g_{y,hkl})^2}{\sigma_y^2} + \frac{(q_z - g_{z,hkl})^2}{\sigma_z^2} \right) \right] \tag{11}$$

with the relative peak widths σ_x, σ_y, and σ_z in each of three mutually orthogonal directions. This peak shape function is useful if the peak widths are determined by finite domain sizes or coherence lengths in the x, y, z-directions.

If the peak widths are determined by the orientational distribution of the unit cells, leading to characteristic arc-shaped peaks, the peak shapes can be factorized into a radial part $L_q(q, g_{hkl})$ depending on the modulus of the scattering vector, and an azimuthal part $L_\psi(q, g_{hkl}, \psi_{hkl})$ depending on the angle $\psi_{hkl} = \arccos(g_{hkl} q/(|g_{hkl}||q|))$ between the scattering vector and the reciprocal lattice vector such that

$$L_{hkl}(q, g_{hkl}) = L_q(q, g_{hkl}) L_\psi(q, g_{hkl}, \psi_{hkl}) \tag{12}$$

The normalized radial peak shape functions are given by

$$L_q(q, g_{hkl}) = \begin{cases} \dfrac{2}{\pi \delta_q} \exp\left[-\dfrac{4(q - g_{hkl})^2}{\pi \delta_q^2} \right] & \text{Gaussian} \\[2ex] \dfrac{\delta_q}{2\pi} \left(1 + \dfrac{4(q - g_{hkl})^2}{\delta_q^2} \right)^{-1} & \text{Lorentzian} \end{cases} \tag{13}$$

where δ_q is the radial peak width which in the case of a Lorentzian is equal to the full width at half maximum (FWHM). For a Gaussian it is related to the standard deviation as $\sigma_q = \sqrt{\pi/8}\delta_q$. Other peak shapes such as Pseudo-Voigt or Pearson VII did not lead to significant improvements in the simulations outlined below.

The normalized azimuthal peak shape functions are given by

$$L_\psi(q, g_{hkl}, \psi_{hkl}) = \begin{cases} \dfrac{1}{2\pi g_{hkl}^2 K(a_{hkl})} \exp\left[-\dfrac{4\psi_{hkl}^2 q^2}{\pi \delta_\psi^2} \right] & \text{Gaussian} \\[2ex] \dfrac{1}{2\pi g_{hkl}^2 K(b_{hkl})} \left(1 + \dfrac{4\psi_{hkl}^2 q^2}{\pi \delta_\psi^2} \right)^{-1} & \text{Lorentzian} \end{cases} \tag{14}$$

with $a_{hkl} = \frac{4 g_{hkl}^2}{\pi \delta_v^2}$ and $b_{hkl} = \frac{4 g_{hkl}^2}{\delta_\psi^2}$. $K(a_{hkl})$ and $K(b_{hkl})$ are normalization functions which are derived in ref. 17 and are given in the Appendix. In the isotropic limit ($a_{hkl}, b_{hkl} \to 0$) the azimuthal peak shape functions reduce to $L_\psi(g_{hkl}) = (4\pi g_{hkl}^2)^{-1}$.

Finite peak widths are related to a limited longitudinal and transverse coherence that could be the result of lattice imperfections such as finite domain sizes or lattice defects, but also the result of instrumental effects such as primary beam wavelength distributions, finite detector resolution, sample aperture and angular spreads. When considering lattice defects and a Gaussian peak shape, there is a direct relationship between the peak width δ_q and the longitudinal coherence length

$$l_l = \frac{4}{\delta_q} \tag{15}$$

Similarly, a relationship between the transverse coherence length and the azimuthal peak width can be derived

$$l_T = \frac{4}{\delta_\psi} \tag{16}$$

In cases where the longitudinal coherence is mainly determined by finite domain size, there should be an approximate relationship $l_l \approx D \approx a^2/\sigma_a$ to the mean domain size D and the mean deviation from the lattice points σ_a of the Debye–Waller factor. In cases where the transverse coherence is mainly determined by the angular distribution of domains, there should be an approximate relationship $l_t \approx D \approx 2a/\tan(2\bar{\delta})$ where $\bar{\delta}$ is the mean deviation angle from the main director orientation.

Eqn (7) and (8) assume an FCC-lattice with perfect ABCA…- or perfect ACBA…-stacking. In some cases such perfect

stacking sequences are not found. To account for more general stacking sequences we factorize the lattice factor $Z(q)$ as

$$Z(q,g) = \frac{(2\pi)^3}{v} \tilde{Z}_\parallel(q,g) \tilde{Z}_\perp(q) \qquad (17)$$

where $\tilde{Z}_\parallel(q)$ is the in-plane lattice factor of the hexagonally close-packed micelles, and $\tilde{Z}_\perp(q)$ is the corresponding lattice factor in the orthogonal direction, normal to the plane. In the plane we assume the reciprocal lattice vectors to be given by

$$a^* = \frac{2\pi}{a} \begin{pmatrix} 1/\sqrt{2} \\ 1/\sqrt{6} \\ 0 \end{pmatrix}, \quad b^* = \frac{2\pi}{a} \begin{pmatrix} 1/\sqrt{2} \\ -1/\sqrt{6} \\ 0 \end{pmatrix} \qquad (18)$$

The in-plane lattice factor is then given by

$$\tilde{Z}_\parallel(q,g) = \sum_{\substack{h,k=-\infty \\ (hk) \neq (000)}}^{\infty} L_{hk}(q, g_{h,k}) \qquad (19)$$

with $g_{hk} = ha^* + kb^*$ and $L_{hk}(q, g_{h,k})$ an anisotropic Gaussian equivalent to eqn (11). Assuming the average distance between adjacent layers to be $t = a/\sqrt{3}$, i.e. that for the ideal close-packing, there are two possible translation vectors

$$t_1 = a \begin{pmatrix} 1/(2\sqrt{2}) \\ 1/(2\sqrt{6}) \\ 1/\sqrt{3} \end{pmatrix}, \quad t_2 = a \begin{pmatrix} 1/(2\sqrt{2}) \\ -1/(2\sqrt{6}) \\ 1/\sqrt{3} \end{pmatrix} \qquad (20)$$

which describe the relative positioning of a micelle from one layer to the next in an in-plane coordinate system with unit vectors $\tilde{e}_x \parallel [111]$, $\tilde{e}_y \parallel [11\bar{2}]$, and $\tilde{e}_z \parallel [1\bar{1}0]$ (see Fig. 1). Assuming that the layer stacking sequence can be described by a first-order Markov process with the two independent probabilities p_{11} and p_{22}, the corresponding lattice factor $\tilde{Z}_\perp(q)$ can be calculated[11,18] and is given in the Appendix.

As shown in Fig. 2, the set $(p_{11}, p_{22}) = (0,1)$ corresponds to twin "B" with perfect ACBA…-stacking (Fig. 2A), (1,0) to twin "A" with perfect ABCA…-stacking (Fig. 2B), (1,1) to a 1 : 1 coexistence of both twins, each with a perfect stacking sequence (Fig. 2C), and (0,0) to perfect ABA…-stacking, i.e. a hexagonally close-packed lattice (HCP). A set (0.5,0.5) corresponds to random stacking where the corresponding scattering pattern is shown in Fig. 2E. Twin coexistence and random stacking both lead to a symmetric hexagonal array of the first order reflections. They differ in that coexisting twins exhibit distinct double peaks on the horizontal layer lines, whereas random stacking leads to single smeared peaks on the layer lines. As the experiments show single smeared peaks at certain scan positions in the gap of the Searle cell, this may be interpreted as random stacking at this position. Single smeared peaks can, however, also be due to a limited coherence in the [111]-direction because of weak positional correlations between micelles in adjacent layers as expressed by eqn (15) and (16). As shown in Fig. 2F, this similarly leads to single smeared peaks, even when assuming coexisting twins. It is thus hard to distinguish between different coherence limitations that lead to peak smearing. Throughout the following we will in such a case model the scattering
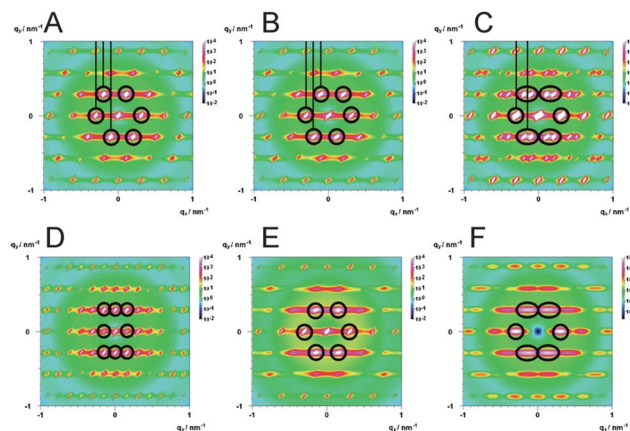

Fig. 2 Calculated scattering patterns for different stacking probabilities (p_{11}, p_{22}): (A) (0,1) corresponding to twin "B", (B) (1,0) to twin "A", (C) (1,1) to coexisting twins, (D) (0,0) to a hexagonally close-packed lattice (HCP), (E) (0.5,0.5) to random stacking, and (F) corresponding to coexisting twins with weak positional correlations of micelles in adjacent (111)-layers. The vertical lines serve to distinguish differences in the peak positions of the two twins.

patterns assuming twin coexistence to have a coherent description for all scattering patterns, but bearing in mind that the assumed model is idealized. Throughout the following we will characterize the volume ratio of the two twins in coexistence regions as $r = V_A/(V_A + V_B)$.

The spatial arrangement of the twinned domains in the gap of the shear cell is schematically shown in Fig. 3. According to ref. 13 we assume the line of highest particle density [210] to be oriented in the shear-direction and the plane normal to the plane of highest particle density (111) oriented in the gradient direction. Thus for the "radial" beam position the primary beam will be parallel to the [111]-direction, whereas for the "tangential" beam position, the beam will be parallel to the [110]-direction.

In the [111]-direction the real space projections of the lattice and the scattering patterns are the same for both twins. This can be seen in model calculations as shown in Fig. 1. We observe the characteristic 6-fold rotational symmetry of the
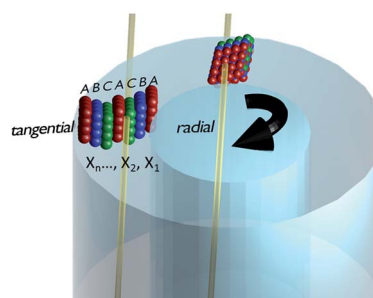

Fig. 3 Configuration twins in the gap of the Searle shear cell. The close-packed (111)-planes of the FCC-lattice are displayed in colours corresponding to those in Fig. 1. The primary beam probes the lattice in the [111]-direction when in the "radial" position, and in the [110]-direction when in the "tangential" position. X_1, X_2, …, X_n indicate different positions that are probed when scanning through the gap of the shear cell.

scattering pattern. In the [110]-direction the real space projections and the scattering patterns of the both twins are different. The scattering patterns for each of both twins are also shown in Fig. 1. We observe the characteristic distorted hexagonal arrangement of the Bragg peaks indicated in Fig. 1. The scattering patterns have 2-fold rotational symmetry. Thus in the [110]-direction, both twins can be clearly distinguished by scattering experiments.

By translating the shear cell from position X_1 to position X_n, a set of n positions in the gap from close to the inner rotor to close to the outer fixed stator can be scanned. For the SANS-experiments $n = 4$, whereas for the synchrotron SAXS-experiments $n = 11$.

Eqn (1) remarkably well describes scattering curves and scattering patterns for a large variety of mesoscopically ordered materials.[17] The use of closed analytical functions facilitates computing and allows efficient implementation into fitting routines. It allows quick extraction of the unit cell size a, the mean deviation from the lattice points σ_a, the nanoparticle radius R, its relative standard deviation σ_R (polydispersity), and the mean size of the crystalline domains D from the measured scattering patterns. Eqn (1) also reproduces correctly secondary Bragg-peaks that appear as a consequence of the finite peak width as outlined in ref. 13. An executable version of the software (*Scatter*)[19] can be obtained from the author.

Results and discussion

Scanning rheo-SANS experiments

Fig. 4A shows the measured SANS pattern in the "radial" beam position, where the neutron beam is parallel to the [111]-direction of the shear-oriented FCC-lattice. The sample is a 16 wt% PI(55)-PEO(170) lyotropic phase after shear-orientation at 500 s^{-1} in the Searle cell. We observe for a lyotropic micellar phase a large number (>50) of Bragg peaks. Most of them are secondary Bragg-peaks, which are crystallographically forbidden, but appear due to their large peak widths and are caused by the small finite domain sizes of the macroscopically oriented crystal.[13]

The model calculation using eqn (1) allows one to obtain the characteristic structural parameters of the FCC crystal. We observe a unit cell dimension of $a = 70$ nm (mean displacement 2 nm), $\sigma_a = 0.03$, and a micellar core radius of $R = 13$ nm (mean relative standard deviation $\sigma_R = 0.10$). The peak shapes can be well described by an anisotropic Gaussian peak shape (eqn (11)) with longitudinal coherence lengths of $l_{210} = l_{110} = 200$ nm and $l_{111} = 90$ nm as derived from the Gaussian peak widths σ_{210}, σ_{110}, and σ_{111} *via* eqn (15). As noted above, in the [111]-direction the scattering patterns of both twins are identical.

Fig. 4B–E show the measured SANS patterns at four different tangential positions when scanning from the edge of the outer stator (position X_4) to the edge of the inner rotor (position X_1).
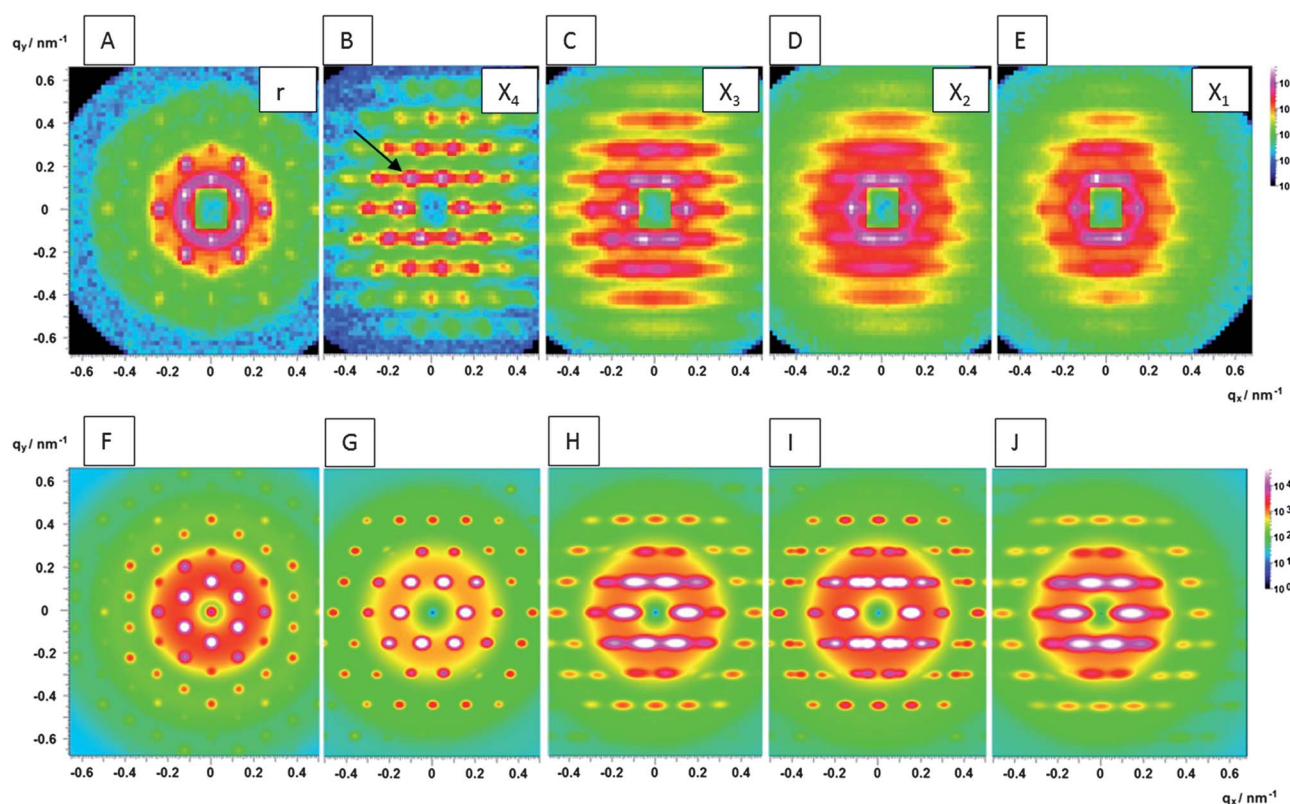

Fig. 4 Rheo-SANS patterns of a shear-oriented FCC phase at 16 wt% PI(55)-PEO(170) in D$_2$O pre-sheared at 500 s^{-1}. (A) "Radial" beam position with the beam in the [111]-direction. (B–E) "Tangential" beam position with the beam in the [110]-direction. Different positions $X_1, \ldots, X_4$ during a scan through the 1 mm gap are indicated. The arrow denotes the upper left first-order reflection, which is shifted to the left for twin "B", and shifted to the right for twin "A". The lower panel (F–J) shows the calculated scattering patterns using eqn (1) with $r = 0.0$ (G), $r = 0.1$ (H), $r = 0.5$ (I), and $r = 0.8$ (J) that fit best to the measured scattering patterns.

The tangential beam position probes the [110]-direction of the shear-aligned FCC-lattice. Also in this direction we observe a large number of Bragg-peaks, which are nearly all primary, *i.e.* crystallographically allowed peaks. For the model calculations we used the structural parameters obtained from the measurement in the [111]-direction in the radial beam position.

SANS patterns at positions between the radial and tangential positions have also been measured. They all can be described by the same structural parameters that have been determined in the radial direction. This indicates that the sample has a homogeneous structure throughout the gap of the shear cell. A detailed analysis of these scattering patterns is the subject of a separate publication.

A characteristic feature of the SANS-pattern measured at the outer gap position X_4 (Fig. 4B) is the distorted hexagon. The upper vertices are shifted to the left, whereas the lower vertices are shifted to the right when compared to a regular hexagon. A comparison to the model calculations in Fig. 1 shows that this is the characteristic scattering pattern expected for twin "B". A calculated scattering pattern with $r = 0.0$, shown in Fig. 4G with the structural parameters obtained from the [111]-direction in Fig. 3B, shows good agreement with the measured scattering pattern.

The scattering pattern measured towards the centre of the gap at position X_3 (Fig. 4C) shows the same distorted hexagon indicative of twin "B". The scattering intensity is higher as now the full beam passes through the gap of the shear cell. A model calculation with $r = 0.1$ is shown in Fig. 4H, showing good agreement with the measured scattering pattern.

At position X_2 in the center of the gap (Fig. 4D) we observe a regular hexagon with considerable smearing in the horizontal direction. As shown in the model calculations in Fig. 1, this is the case if both twins occur with equal probability, expected at the location of the twin boundary surface. The corresponding calculated scattering pattern ($r = 0.5$) is again in good agreement with the experiment.

The scattering pattern measured at position X_1 at the inner part of the gap close to the rotor (Fig. 4E) shows a distorted hexagon, but now the upper vertices are shifted to the right, whereas the lower vertices are shifted to the left compared to a regular hexagon. This is the characteristic scattering pattern expected for twin "A". The peaks are considerably smeared horizontally, which at this gap position is also due to the beam path probing the FCC-lattice and both twins with slightly different orientations due to the curvature of the shear cell. In the model calculation this is accounted for by using $r = 0.8$ for twin "A". Using this ratio, again good agreement between the measured and calculated scattering pattern was obtained.

This series of SANS-measurements and 4 more series on other FCC-samples compiled in the ESI† show that macroscopic "Siamese" twins are formed in the gap of the shear cell with twin "B" always on the outside and twin "A" always on the inside close to the inner rotor.

Scanning synchrotron rheo-SAXS experiments

To scan the gap with higher resolution, we performed synchrotron SAXS experiments at the beamline ID02 at ESRF,

Grenoble. Similar to the upper series of experiments, we first probed the sample in the radial direction, where the beam is parallel to the [111] direction of the FCC-lattice (Fig. 5A). The sample was a 15 wt% PI(62)-PEO(193) lyotropic phase after shear orientation in a Searle cell with a shear rate of 750 s^{-1}. Again, we observe a large number of Bragg peaks.

A model calculation is also shown, from which the most important structural parameters are obtained. We observe a unit cell dimension of $a = 85$ nm (mean displacement $\sigma_a = 0.001$), and a micellar core radius of $R = 15$ nm (mean relative standard deviation $\sigma_R = 0.10$). The peak shapes can be well described by the Gaussian radial and azimuthal peak shape function (eqn (13) and (14)) with a domain size of $D = 950$ nm and a transverse coherence length of $l_t = 300$. The much smaller radial peak widths of the SAXS-patterns in comparison to the SANS-patterns indicate that the radial peak width or longitudinal coherence in the SANS-patterns is mainly limited by the finite coherence of the neutron beam and not by the sample domain size.

With the synchrotron X-ray beam we were able to probe 11 different positions in the gap at the tangential beam position, *i.e.* the [110] direction of the FCC-lattice. 6 representative scattering patterns are shown in Fig. 5B–G. The whole set of scattering patterns is shown in the ESI (Fig. S5†). Compared to the SANS-patterns, the SAXS-patterns are tilted by 90°, which is due to the ID02 data format used and has been considered in the model calculations.

The scattering pattern shown in Fig. 5B was measured at the outer position of the gap at position X_{11}. We observe as a characteristic feature a distorted hexagon, where the left vertices are shifted downwards and the right vertices are shifted upwards compared to a regular hexagon. This corresponds to the scattering pattern of twin "B". A model calculation ($r = 0.0$) is shown in Fig. 5I and again shows good agreement with the measured scattering pattern, using the same structural parameters as for the radial scattering pattern, *i.e.* along the [111]-direction. The scattering pattern measured towards the centre of the gap at position X_4 (Fig. 5C) shows the same distorted hexagon indicative of twin "B". The scattering intensity is higher as the full beam passes through the gap of the shear cell.

The SAXS-pattern shown in Fig. 5D is measured in the central gap region at position X_5, where similar to Fig. 5C a symmetric hexagon is observed, indicating the location of the twin boundary surface ($r = 0.5$). Further towards the inner region at position X_8 (Fig. 5E) a distorted hexagon, now with the left vertices shifted upwards and the right vertices shifted downwards compared to a regular hexagon, is observed. This indicates the presence of twin "A". The model calculation with $r = 0.8$ is again in good agreement with the scattering pattern. The same scattering pattern is observed at all remaining positions up to X_1 at the inner part of the gap. The location of twin "B" on the outside is also found for another sample series using synchrotron SAXS as shown in the ESI (Fig. S5†).

Fig. 6 illustrates the experimental findings. On the outer side of the gap, we always observe twin "B", in the middle of the gap there is a coexistence of both of the twins with the twin boundary surface, while on the inner side of the gap we always observe twin
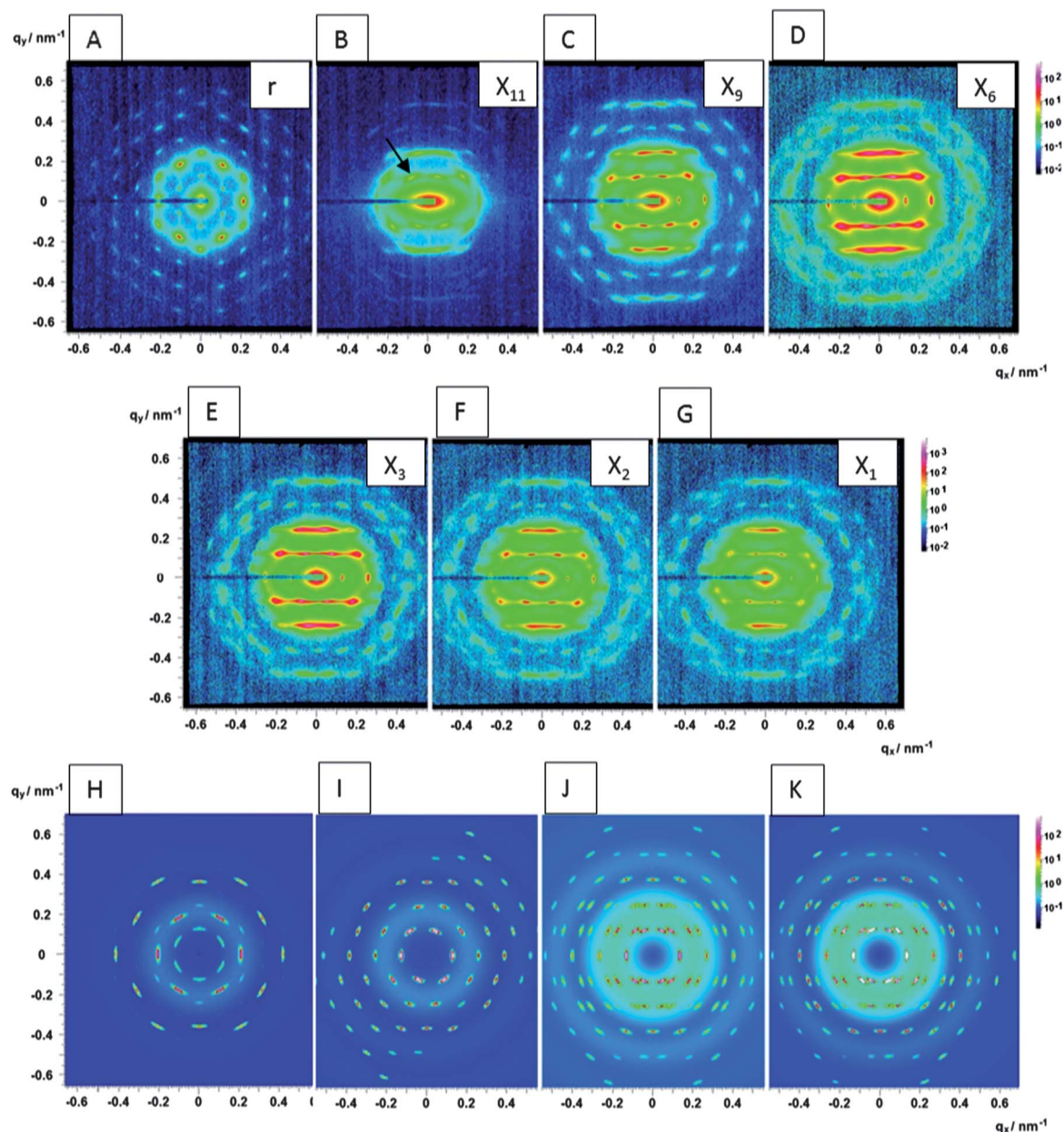
Fig. 5 Synchrotron rheo-SAXS patterns of a shear-oriented FCC phase at 15 wt% PI(62)-PEO(193) in H_2O presheared at 750 s^{-1}. (A) "Radial" beam position with the beam in the [111]-direction. (B–G) "Tangential" beam positions with the beam in the [110]-direction. Different positions $X_1, ..., X_{11}$ during a scan through the 1 mm gap are indicated. The arrow denotes the lower left first-order reflection, which is shifted downwards for twin "B", and shifted upwards for twin "A". The lower panel (H)–(K) shows the calculated scattering patterns using eqn (1) with $r = 0.0$ (I), $r = 0.5$ (J), and $r = 0.9$ (K) that fit best to the measured scattering patterns.
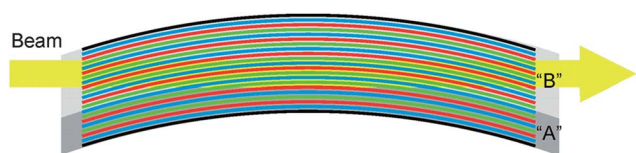

Fig. 6 Arrangement of layers in the gap of the shear cell. Twins "A" and "B" are separated by a twin boundary surface approximately in the center of the gap. Also indicated is the dimension of the primary beam that may pass both twins depending on the z-position within the gap.

"A". We did not observe a random occurrence of the twins in the inner and outer parts of the gap, as in the studies of Molino *et al.*, which we attribute to a different and more well-defined shear protocol that induces twin formation in our study. The ratios r measured at the inner side of the gap never approach a value $r = 1.0$, since the beam also passes regions with twin "B" when transecting the gap as indicated in Fig. 6.

Transmission electron microscopy

The scattering experiments indicate that twinning is a very prominent defect in highly sheared soft crystals. To visualize
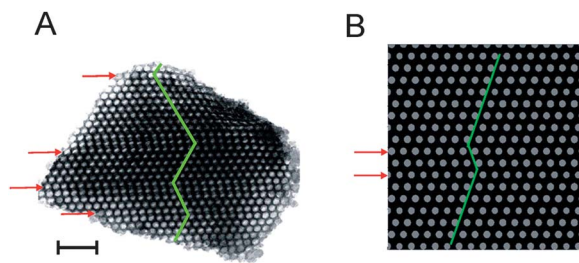
Fig. 7 (A) TEM-image of a small piece of a mesoporous solid replica of the lyotropic FCC phase showing twinning. The location of the twin boundary surfaces is denoted by the arrows. The green line with kinks serves to visualize the boundary surfaces within the sample. (B) shows a corresponding simulated projection in the [110]-direction. The scale bar is 100 nm.[20]

Fig. 8 Synchrotron SAXS patterns of a shear-oriented lyotropic phase of polystyrene-coated Fe_2O_3-nanoparticles (diameter 16.6 nm) at a concentration of 50 wt% with a twin ratio "B"/"A" of 0.9. Measurements are shown on the left, and the calculation using eqn (1) is shown on the right.

such twin boundary surfaces directly, we performed transmission electron microscopy. To prepare a stable replica of the lyotropic phase we used a sol–gel process that has been outlined previously.[13] We investigated samples that had been shear-aligned by using a doctor blade on a glass slide. This procedure does not exactly correspond to the shear protocol in our rheo-SANS and rheo-SAXS-studies, but still produces large single domain samples at high shear rates. The samples were then solidified by addition of pre-hydrolyzed tetramethoxysilane (TMOS), calcination and grinding in a mortar to obtain small micron-sized pieces that could be imaged by transmission electron microscopy (TEM).

Fig. 7 shows the TEM-image of a small piece of a lyotropic phase replica. The crystal is viewed from the 110-direction which allows us to distinguish both twins. We observe the characteristic twin boundary surfaces, whose locations are indicated in Fig. 6. Also shown is a simulated projection of the mesoporous FCC-crystal in the [110]-direction with two twin-boundary surfaces. The line containing the two kinks serves to visualize the location of the boundary surfaces.

Shear-oriented lyotropic nanoparticle lattices

We recently discovered that polymer-coated nanoparticles can also form highly ordered lyotropic liquid crystalline phases.[12] These polymer-coated nanoparticles have a well-defined core–shell structure, the core being the nanoparticle and the shell being the solvent-swollen polymer brush. This very much resembles the core–shell structure of block copolymer micelles, which have a core of the insoluble polymer blocks, and a solvent-swollen shell of the soluble blocks. Due to the structural similarity we expected a similar behaviour upon shear deformation. Since well-defined polymer coated, monodisperse nanoparticles were available only in small amounts, we used co-axial thin glass-capillaries to shear-align small volumes of samples by rotating the inner capillary with respect to the stationary outer capillary, similar to the rheo-SANS and rheo-SAXS experiments described above. For this shear-experiment only ca. 200 μL of sample was needed. The structure of the shear-aligned sample was then investigated by synchrotron-SAXS.
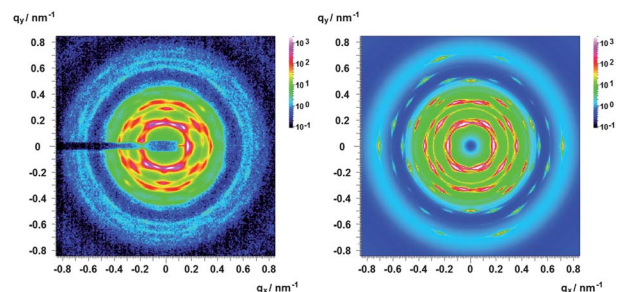
Fig. 8 shows the measured scattering pattern when passing the X-ray beam through the outermost part of the gap between the two capillaries. Due to the large gap curvature it is not possible with this capillary setup to selectively probe different regions in the gap with high resolution. Still, the scattering pattern in Fig. 8 measured at the outer edge of the gap clearly shows twinning with the preference (90%) for twins "B". From model calculations we could determine the structural parameters of the lyotropic gel. We observe a unit cell dimension of $a = 61$ nm (mean displacement $\sigma_a = 0.03$), a nanoparticle radius of $R = 8.0$ nm (mean relative standard deviation $\sigma_R = 0.04$). The peak shapes can be well described by a Lorentzian radial and azimuthal peak shape function (eqn (13) and (14)) with a domain size of $D = 400$ nm and a transverse coherence length of $l_t = 60$ nm.

Our experiments show that for soft FCC-crystals sudden cessation of shear after shearing at high shear rates leads to the formation of macroscopically separated "Siamese" twins with twin B always located in the outside region of the gap, close to the outer stator, whereas the other twin "A" is always located in the inside region of the gap, close to the inner rotor. We could locate the twin boundary surface always in the centre region of the gap, somewhat more towards the inner part of the gap.

Growth mechanism

The observed shear-induced formation of macroscopic "Siamese" twins is a surprising phenomenon. Usually, samples will contain many small twinned-domains giving rise to some specific texture in the diffraction pattern. In the following we propose a possible mechanism for the formation of macroscopic twins. We use an analogy to deformation twinning, an important mode of plastic deformation known for metals,[21] which has recently received considerable attention, because it occurs without breaking which is interesting for crash energy absorption and industrial deep drawing and forging processes.[22]

Twinning is typically observed in plastically deformed metals at low temperatures and high shear rates. Twins nucleate at stacking faults and materials with low stacking fault energy have a high tendency to form twins. The velocity of twin plate propagation is higher than for any other dislocation motion. Twinning is thus an important deformation mode for very fast
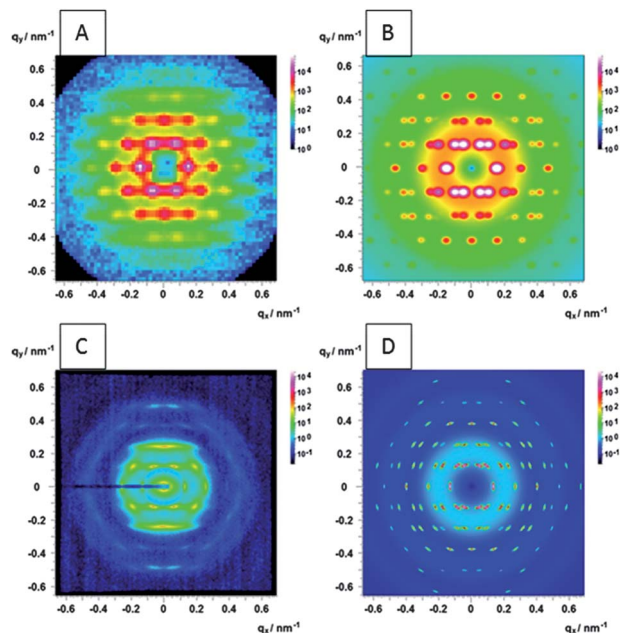
Fig. 9 (A) Rheo-SANS (PI(55)-PEO(170)) and (C) rheo-SAXS (PI(62)-PEO(193)) scattering patterns measured in the "tangential" beam position during pre-shearing at 500 s^{-1} of the FCC-phase. A regular hexagonal arrangement of the first-order peaks is observed, indicating no preferred twin-formation. (B) and (D) show the corresponding model calculations. The measured scattering patterns are the same at all positions in the gap.

and high mechanical strains, *i.e.* conditions where other slip systems cannot accommodate the deformation.[22,23] With time, the twinning plate grows thicker through the formation of twinning dislocation dipoles on the plate surfaces.

In our experiments, all macroscopic twin structures were induced by first shearing the sample at high shear rates under continuous shear. Under these conditions a constant and stationary velocity gradient is established. A "layer sliding" mechanism has been proposed for the mutual movement of the hexagonally close-packed (111)-layers of the micelles in shear direction [110] during shear.[5–7] This is confirmed in our experiments. When measuring the scattering patterns during shear in the tangential beam position (Fig. 9) we always observe a regular hexagon at all gap positions.
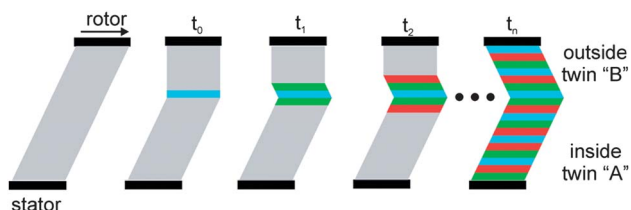

Fig. 10 Development of a macroscopic twin after sudden cessation of shear in the gap of a Searle cell. The sudden stop of the upper rotor leads to large shear strains in the still moving layers in the center of the gap. At some point a critical strain is reached that induces fast deformation twinning which quickly relieves local stress. The twins grow towards the outer regions of the gap until a macroscopic "Siamese" twin has been formed.

When the rotor is suddenly stopped, this temporarily results in locally very high shear rates and shear strains in the centre of the gap. Fig. 10 schematically shows the layer stacks in the gap between the rotor (top) and the stator (bottom). During the initial shearing-period at times $t < t_0$ adjacent planes move by layer-sliding with no defined stacking sequence, indicated by the grey colour, and an affine shear strain is established across the gap. After stopping the rotor at $t = t_0$, at some position in the gap the strain reaches a critical value to induce deformation twinning. This mechanism will relieve the strain in a fast and stepwise manner. The resulting stacking sequence corresponds to a macroscopic "Siamese" twin as observed in the experiment. Why twin "B" is always formed outside remains still unclear. In any case, we observe that very high shear rates ≥ 500 s^{-1} are necessary to obtain macroscopic twins. When lower shear rates are used (*e.g.* 200 s^{-1} as shown in Fig. S3 in the ESI†), Debye–Scherrer rings – indicating less well-defined and well-oriented layer-stacking – are observed in the central part of the gap.

Conclusions

Using a well-defined shear protocol we find by using rheo-SANS and synchrotron rheo-SAXS that at high deformation rates soft FCC colloidal crystals form macroscopic "Siamese" twins in the gap of the shear cell with one twin always located in the outer region of the gap, close to the outer stator, and the other twin always located in the inner region of the gap, close to the inner rotor. The twin boundary surface could be located in the centre region of the gap. The measured scattering patterns could be quantitatively described to obtain the structural characteristics of the FCC-twin structures. We could directly visualize twin boundary surfaces by using transmission electron microscopy on vitrified samples and found macroscopic twinning also in sheared nanoparticle supercrystal lattices. In analogy to the plastic deformation of nanocrystalline metals we propose a mechanism for the formation of such macroscopic twins.

Appendix

Peak shape normalization functions

The normalization function $K(a)$ is given by an integral of a Gaussian over the deviation angle ψ and can for small a be approximated *via* a series expansion of the exponential, *i.e.*

$$K(a) = \int_0^\pi e^{-a\psi^2} \sin\psi \, d\psi = \sum_{n=0}^\infty \frac{(-1)^n a^n}{n!} \int_0^\pi \psi^{2n} \sin\psi \, d\psi$$

$$= 2 - (\pi^2 - 4)a + \frac{(48 - 12\pi^2 + \pi^4)a^2}{2}$$

$$- \frac{(-1440 + 360\pi^2 - 30\pi^4 + \pi^6)a^3}{6} + \cdots \quad \text{(A1)}$$

For large a the integral can be approximated *via* the series expansion of the sine-function, *i.e.*

$$K(a) = \int_0^\pi e^{-a\psi^2} \sin\psi \, d\psi$$

$$= \sum_{n=0}^\infty \frac{(-1)^n}{(2n+1)!} \int_0^\pi e^{-a\psi^2} \psi^{2n+1} d\psi$$

$$= \sum_{n=0}^\infty \frac{(-1)^n}{(2n+1)!} \frac{(\Gamma[n+1] - \Gamma[n+1, a\pi^2])}{2a^{n+1}}$$

$$= \frac{\left(1 - e^{-a\pi^2}\right)}{2a} - \frac{1 - e^{-a\pi^2}(1 + a\pi^2)}{12a^2}$$

$$+ \frac{2 - e^{-a\pi^2}(2 + 2a\pi^2 + a^2\pi^4)}{240a^3}$$

$$- \frac{6 - e^{-a\pi^2}(6 + 6a\pi^2 + 3a^2\pi^4 + a^3\pi^6)}{10\,080a^4} + \cdots \quad (A2)$$

The normalization function $K(b)$ is given by an integral of a Lorentzian over the deviation angle ψ and can for small b also be approximated *via* a series expansion of the exponential, *i.e.*

$$K(b) = \int_0^\pi \frac{1}{1 + b\psi^2} \sin\psi \, d\psi$$

$$= \sum_{n=0}^\infty (-1)^n b^n \int_0^\pi \psi^{2n} \sin\psi \, d\psi =$$

$$= 2 - (\pi^2 - 4)b + (48 - 12\pi^2 + \pi^4)b^2$$

$$- (-1440 + 360\pi^2 - 30\pi^4 + \pi^6)b^3 + \cdots \quad (A3)$$

At high b the integral can be approximated *via* the series expansion of the sine-function, *i.e.*

$$K_3(b) = \int_0^\pi \frac{1}{1 + b\psi^2} \sin\varphi \, d\varphi$$

$$= \sum_{n=0}^\infty \frac{(-1)^n}{(2n+1)!} \int_0^\pi \frac{1}{1 + b\psi^2} \psi^{2n+1} d\psi$$

$$= \sum_{n=0}^\infty \frac{(-1)^n}{(2n+1)!} \frac{\pi^{2n+1}{}_2F_1[1, n+1, n+2; -b\pi^2]}{(2n+1)}$$

$$\times \frac{\ln(1 + b\pi^2)}{2b} - \frac{b\pi^2 - \ln(1 + b\pi^2)}{12b^2}$$

$$+ \frac{-2b\pi^2 + b^2\pi^4 + 2\ln(1 + b\pi^2)}{480b^2} -$$

$$= \frac{b\pi^2(6 - 3b\pi^2 + 2b^2\pi^4) - 6\ln(1 + b\pi^2)}{60\,480b^4} + \cdots$$

$$(A4)$$

Lattice factor for statistically stacked layers

$$\tilde{Z}_\perp(q) = \frac{s_1}{c_1(c_2 + c_3 + c_4 + c_5)}$$

$$s_1 = 2(p_{11} - 1)(p_{22} - 1)(p_{11} + p_{22}) \sin^2\left[(x_1 - x_2)/2\right]$$

$$c_1 = p_{11} + p_{22} - 2$$

$$c_2 = -1 + p_{11}(1 - p_{11}) + p_{22}(1 - p_{22}) - p_{11}p_{22}$$

$$c_3 = (p_{22}(p_{22} - 1) + p_{11}(p_{22} + 1))\cos(x_1)$$

$$c_4 = (p_{11}(p_{11} - 1) + p_{22}(1 + p_{11}))\cos(x_2)$$

$$c_5 = (1 - p_{11} - p_{22})\cos(x_1 + x_2) - p_{11}p_{22}\cos(x_1 - x_2)$$

$$x_1 = a\left(\frac{1}{2}q_x + \frac{1}{2\sqrt{3}}q_y + \sqrt{\frac{2}{3}}q_z\right)$$

$$x_2 = a\left(\frac{1}{2}q_x - \frac{1}{2\sqrt{3}}q_y + \sqrt{\frac{2}{3}}q_z\right)$$

(A5)

Notes and references

1 I. W. Hamley, *Introduction to Soft Matter: Polymers, Colloids, Amphiphiles, and Liquid Crystals*, Wiley, 2000.

2 R. A. L. Jones, *Soft Condensed Matter Physics*, Oxford University Press, Oxford, 2002.

3 T. A. Witten and P. A. Pincus, *Macromolecules*, 1986, **19**, 2509.

4 J. Buitenhuis and S. Förster, *J. Chem. Phys.*, 1997, **107**, 262.

5 B. J. Ackerson, J. B. Hayter, N. A. Clark and L. Cotter, *J. Chem. Phys.*, 1986, **84**, 2344.

6 W. Loose and B. J. Ackerson, *J. Chem. Phys.*, 1994, **101**, 7211.

7 G. A. McConnell, M. Y. Lin and A. P. Gast, *Macromolecules*, 1995, **28**, 6754.

8 I. W. Hamley, *J. Phys.: Condens. Matter*, 2001, **13**, R643.

9 O. Diat, G. Porte and J.-F. Berret, *Phys. Rev. B: Condens. Matter Mater. Phys.*, 1996, **54**, 14869.

10 F. R. Molino, J.-F. Berret, G. Porte, O. Diat and P. Lindner, *Eur. Phys. J. B*, 1998, **3**, 59.

11 J. Jiang, C. Burger, C. Li, J. Li, R. H. Colby, M. H. Rafailovich and J. C. Sokolov, *Macromolecules*, 2007, **40**, 4016.

12 S. M. Taheri, S. Fischer, M. Trebbin, S. With, J. H. Schröder, J. Perlich, S. V. Roth and S. Förster, *Soft Matter*, 2012, **8**, 12124.

13 S. Förster, A. Timmann, C. Schellbach, A. Frömsdorf, A. Kornowski, H. Weller, S. V. Roth and P. Lindner, *Nat. Mater.*, 2007, **6**, 888.

14 P. Lindner, R. P. May and P. A. Timmis, *Phys. B*, 1992, **180–181**, 927; K. Lieutenant, P. Lindner and R. Gähler, *J. Appl. Crystallogr.*, 2007, **40**, 1056–1063.

15 P. Panine, M. Gradzielski and T. Narayanan, *Rev. Sci. Instrum.*, 2003, **74**, 2451–2455.

16 S. Förster, A. Timmann, M. Konrad, C. Schellbach, A. Meyer, S. S. Funari, P. Mulvaney and R. Knott, *J. Phys. Chem. B*, 2005, **109**, 1347.

17 S. Förster, S. Fischer, K. Zielske, C. Schellbach, M. Sztuki, P. Lindner and J. Perlich, *Adv. Colloid Interface Sci.*, 2011, **163**, 53–83.

18 S. Hendricks and E. Teller, *J. Chem. Phys.*, 1942, **10**, 147.

19 S. Förster, L. Apostol and W. Bras, *J. Appl. Crystallogr.*, 2010, **43**, 6860.

20 C. Schellbach, Ph.D. thesis, University of Hamburg, 2008.

21 J. W. Christian and S. Mahajan, *Prog. Mater. Sci.*, 1995, **39**, 1–157.

22 J. Marian, W. Cai and V. V. Bulatov, *Nat. Mater.*, 2004, **3**, 158.

23 M. Chen, E. Ma, K. J. Hemker, H. Sheng, Y. Wang and X. Cheng, *Science Express Report, 9.7.*, 2007.